Non-Equilibrium Carrier Transport in Quantum Dot Heterostructures

Mengxia Liu,[‡] Sachin D. Verma,[‡,§] Zhilong Zhang,[‡] Jooyoung Sung,[‡,#] Akshay Rao[‡*]*

[‡]Cavendish Laboratory, University of Cambridge, JJ Thomson Avenue, Cambridge CB3 0HE, United Kingdom.

[§]Department of Chemistry, Indian Institute of Science Education and Research Bhopal, Bhopal Bypass Road, Bhopal 462066, Madhya Pradesh, India.

[#]Department of Emerging Materials Science, Daegu Gyeongbuk Institute of Science and Technology, Daegu 42988, Republic of Korea

KEYWORDS: Quantum dots, non-equilibrium carrier transport, ultrafast dynamics, transient absorption microscopy

ABSTRACT: Understanding carrier dynamics and transport in quantum dot based heterostructures is crucial for unlocking their full potential for optoelectronic applications. Here we report the direct visualisation of carrier propagation in PbS CQD solids and quantum-dot-in-perovskite heterostructures using femtosecond transient absorption microscopy. We reveal three distinct transport regimes: an initial super-diffusive transport persisting over hundreds of femtoseconds, an Auger-assisted sub-diffusive transport before thermal equilibrium is achieved, and a final hopping regime. We demonstrate that the super-diffusive transport lengths correlate strongly with the degree of energetic disorder and carrier delocalization. By tailoring the

perovskite content in heterostructures, we obtained a super-diffusive transport length exceeding 90 nm at room temperature and an equivalent diffusivity of up to 106 $cm^2\ s^{-1}$, which is four orders of magnitude higher than the steady-state values. These findings introduce promising strategies to harness non-equilibrium transport phenomena for more efficient optoelectronic devices.

Quantum dot and quantum well architectures, which exhibit tunable optical transitions through the confinement of carriers at the nanoscale, are attractive building blocks for optoelectronics. Colloidal quantum dots (CQDs) – semiconductor nanocrystals that benefit from solution processing at low temperatures – show promise for the scalable manufacturing of large-area optoelectronic devices[1,2]. Rapid advances in materials processing have driven impressive performance progress, but challenges remain to achieve full control over electronic properties. Carrier mobilities in CQDs are typically low ($\sim 10^{-3}$–10^{-2} $cm^2\ V^{-1}\ s^{-1}$)[3]. Disorder and defects – consequences of low-temperature solution processing – are inevitably present in CQD ensembles, in which their abundance results in an inhomogeneous energy landscape and carrier losses[4,5]. These intrinsic drawbacks in disordered semiconductors affect the transport of excitons and charges and, therefore, limit device performance.

A novel type of heterostructure, one that integrates colloidal nanocrystals epitaxially into a perovskite matrix, offers an additional degree of freedom to control charge transport and recombination for more efficient optoelectronic devices[6,7]. This quantum-dot-in-perovskite (QDiP) heterostructure takes advantage of the compelling carrier transport properties of metal-halide perovskites as well as the wide spectral tunability of quantum dots[8]. They exhibit

electronic and transport properties programmed at the nanoscale. By engineering the composition and microscopic structure, QDiP materials can be tailored to deliver improved carrier mobility or enhanced radiative recombination[9,10]. These open new possibilities for optoelectronic devices[10,11]. However, the fundamental nature of carrier transport in such systems remains elusive. It is unclear whether the electronic coupling strength is sufficient to generate electronic bands, and how the transport mechanism is affected by the fluctuating energy landscape.

Recent advances have been made towards understanding exciton and charge transport via contactless optical techniques. The charge transfer in halide-passivated PbS CQDs has been studied via a donor-acceptor method using transient absorption spectroscopy, demonstrating a spatially averaged mobility below 0.1 $cm^2 V^{-1} s^{-1}$ and an inter-dot hopping time of ~8 ps for 3.2 nm dots[12]. Time-resolved photoluminescence (PL) microscopy has been exploited to probe exciton transport in CQD solids on nanosecond timescales and reveal the exciton hopping mechanism with a time-dependent diffusivity due to downhill energy migration[13]. These methods, however, cannot elucidate the ultrafast spatial dynamics due to the lack of suitable combinations of spatial precision and temporal resolution. Thus, the early time non-equilibrium dynamics of CQD solids remains unexamined.

Here we report a direct visualisation of carrier transport in CQD and QDiP solids using ultrafast transient absorption microscopy (TAM) with 10 fs temporal resolution and 10 nm spatial precision (Figure 1a), and reveal a multi-stage transport mechanism. At early times following photoexcitation super-diffusive transport was observed to correlate with inter-particle spacing and the degree of energetic disorder. The super-diffusive transport regime can be adjusted by incorporating CQDs into perovskite matrix at different ratios, resulting in a maximum transport length of 90 nm and significant diffusivities of up to 106 $cm^2 s^{-1}$. Over tens

of picoseconds, an Auger-assisted transport for hot carriers takes place, which is then followed by a slower sub-diffusive transport for thermally relaxed carriers. These insights suggest a direct route to optimise the design of heterostructures and improve the performance of CQD-based optoelectronics.

RESULTS AND DISCUSSION

We focused our investigation on the ultrafast spatio-temporal dynamics of densely packed PbS CQD and QDiP solids. The PbS quantum dots were synthesised and exchanged with halide ligands as reported previously, and the size of CQDs is tuned to yield an exciton peak at ~850 nm in solution (Figure S1a, S1b, Methods)[9]. Without the introduction of perovskite matrix, the exchanged CQDs form randomly-packed ensembles with a high packing density of ~64% (ref.[14]) and a tiny inter-dot separation (l = 2 – 4 Å, ref.[15]). The exciton absorption peak of CQD film is red-shifted by 91 meV compared with that of colloidal solution, indicating the partial relaxation of quantum confinement due to strong electronic coupling among dots. For QDiP systems, the pre-exchanged CQDs were incorporated into a perovskite matrix consisting of $CsPbBr_2I$, where the bromide and iodide ratio has been optimised to achieve an ideal lattice matching with embedded PbS CQDs (Figure 1b). X-ray diffraction patterns of QDiP films confirm the lattice matching between the two components (Figure S1c). The transmission electron microscopy image of QDiP heterostructures demonstrate the successful incorporation of perovskite matrix and the epitaxially-aligned interfaces (Figure S1d). By tuning the concentration of perovskite, we are able to tailor the average dot-to-dot separation length (Figure 2a, 2b). At low perovskite concentration (< 36% volume percentage), the matrix fills in the voids among CQDs without noticeably separating the dots, evidenced by a negligible shift of the exciton peak. As the perovskite ratio increases, larger inter-dot spacing is achieved, resulting in

reduced electronic coupling and, therefore, a blue-shift of PbS exciton absorption peak in comparison to pure CQD films (Figure 2c).

The two-dimensional transient absorption maps show the ground-state bleach (GSB) bands of perovskite and CQDs – centred at 565 nm and 905 nm, respectively – as well as a broad photoinduced absorption (PIA) band centred at 670 nm (Figure 2d, S2, S3). This PIA feature is assigned to the intraband transitions or excited state absorption in CQDs – in particular the transitions associated with 1P states[16-18].

Upon photoexcitation above the bandgap of perovskite, carriers are generated in both constituents. The excited carriers in CQDs move energetically downhill to the lowest-energy sites, resulting in a red-shift of the CQD bleach peak. The width of shift is determined by the degree of energetic disorder – which can be quantified by the width of inhomogeneous broadening of site energy, σ_{inh} – and the available thermal activation in the system, given by the equation,

$$\Delta E = -\frac{\sigma_{inh}^2}{2k_B T},$$

where ΔE represents the energy difference before and after thermalisation, k_B is the Boltzmann constant, and T is temperature[4,19]. By comparing the energy shifts for different samples, we reveal a decrease in inhomogeneous broadening as the perovskite content increases (Figure 2e). This indicates that the incorporation of lattice-matched perovskite allows for an improved energy landscape in CQDs.

In addition, the excited carriers generated from perovskite inject into CQDs within a few picoseconds, as evidenced by the observation of identical time constants between the decay of GSB band of perovskite and the rise of GSB band of CQDs (Figure S4). On the other hand, the corresponding rise components are absent in the kinetic profile for the PIA band at 670 nm,

indicating clearly that the observed PIA band is insensitive to the injected carriers. This enables us to track, by probing at the PIA band, the motion of carriers that are solely generated within and transport through CQDs, ruling out the carrier movement taking place in perovskite.

We then directly visualised the spatial carrier dynamics of QDiP heterostructures by performing TAM measurements. We combined ultrafast transient absorption spectroscopy and a high-performance optical microscope to deliver simultaneously extreme temporal resolution (10 fs) and nanoscale localisation (Figure 1a)[20]. A near-diffraction-limited pump pulse, centred at 580 nm, was used to excite the sample, generating a gaussian shaped excited carrier distribution (Figure S5)[21]. A time-delayed wide-field probe pulse was applied to spatially resolve the transient response and therefore monitor the distribution of carrier population as a function of time. These enable us to track – by comparing the recorded images – the evolution of photoinduced dynamics with sub-10 nm spatial precision, which is limited only by the signal-to-noise characteristics of the system (see Methods, Supplementary note S1, S2)[22,23].

The measurements were carried out at multiple excitation intensities, with a minimum of $\langle N_{abs} \rangle = 0.045$ to maintain a signal-to-noise ratio. $\langle N_{abs} \rangle$ is the average number of photons absorbed per CQD[24], obtained from the product of the absorption cross-section and the fluence per pulse[25,26]. By probing close to the PIA peak at 690 nm, we obtained a series of TAM images that allow us to exclusively monitor the distribution of carriers generated in CQDs. The TAM images were fitted with isotropic two-dimensional Gaussian function as the initially generated carrier distribution closely resembles the diffraction-limited pump and the spatial expansion occurs isotropically (Figure S6)[22,27]. This enables us to extract the variance of carrier distribution at a certain time, σ_t^2, and quantify the spatio-temporal evolution by calculating the mean-square-displacement, $MSD = \sigma_t^2 - \sigma_0^2$.

The time evolution of MSD obtained from densely packed CQD solids reveals multiple distinct regimes for carrier transport (Figure 3a). Following photoexcitation, the excited carriers are spatially distributed within the pump area (Figure S6b), showing a σ_0 of 141 ± 10 nm close to the diffraction limit of the microscope (133 nm). Within a few hundreds of femtoseconds, the excited carriers undergo a pronounced spatial expansion with a diffusion exponent (α) slightly larger than 1, indicative of a super-diffusive motion (as described by $MSD \propto t^{\alpha}$, $\alpha > 1$) and a time-dependent diffusivity. After the initial expansion (> 400 fs), the broadening of carrier distribution becomes progressively slower and the MSD is observed to grow sub-linearly ($\alpha < 1$).

This later-time sub-linear growth of MSD is consistent with previous observations via time-resolved PL microscopy[13] and indicates the sub-diffusive transport resulting from site-to-site carrier hopping in CQD ensembles. The carriers migrate energetically downhill over the disordered energy landscape, resulting in decreased hopping rates with time.

The early-time transport, however, has not been observed previously in CQD solids. We calculated the diffusivity of carriers as $D(t) = MSD(t)/2t$ (ref.[13]) and extracted, for the initial transport, a maximum transient diffusivity of 102 $cm^2\ s^{-1}$ at the lowest pump fluence (Figure 3b). This non-equilibrium diffusivity corresponds to an equivalent carrier mobility of 3.94×10^3 $cm^2\ s^{-1}\ V^{-1}$ – which is about four orders of magnitude higher than their mobility at equilibrium[12,28,29]. These observations suggest that the super-diffusive transport is accessed at the earliest times when carriers are delocalized and move freely with little scattering. This regime – though persisting for only ~300 fs – allows carriers to propagate over a significant distance of 80 nm, which corresponds to ~26 dots (Figure 3c). We further compare the carrier velocity in CQDs to their theoretical group velocity, the speed with which a wave packet moves in lattice. An initial carrier velocity of 450 m s^{-1} is estimated from the time-evolution of carrier transport length. This

is substantially lower than the theoretical group velocity of PbS (9×10^5 m s^{-1} for an electron and 6×10^5 m s^{-1} for a hole)[30]. The comparison suggests that, despite the high diffusivity, the non-equilibrium carrier movement through PbS CQDs is much slower than the propagation of wave packets in a perfect (inelastic-scattering free) PbS crystal.

Fluence-dependent measurements further elucidate the effect of carrier density on transport dynamics (Figure 3a, 3b). As $<N_{abs}>$ increases from 0.045 to 0.18, a higher concentration of free carriers is generated, triggering Auger recombination (Figure S7)[31,32]. For the super-diffusive regime, we observed that the diffusivity decreases at higher pump fluence, suggesting that the carrier-carrier scattering limits the transport process. For the following sub-diffusive transport, two different regimes are distinguished. On the timescale of Auger recombination process (<100 ps), MSD increases significantly with pump fluence (the artificial broadening of σ is negligible up to 100 ps, supplementary note S3)[33,34]. We attribute this positive scaling of MSD with pump fluence to an Auger-assisted carrier transport. Here, the Auger process generates energetic charge carriers with excess kinetic energy, which assists in overcoming the potential barriers and energetic fluctuations, and thus contributes to an increased hopping rate. These carriers subsequently relax over tens of picoseconds to reach thermal equilibrium with the lattice. When carriers are completely cooled (>100 ps), a fluence-independent hopping regime takes over[35].

Previous studies have explored sub-diffusive transport in CQD solids and elucidated the role of energetic disorder and inter-dot spacing in controlling the hopping process[13]. The super-diffusive transport process, however, has not been explicitly studied. To investigate the factors that influence the distance of super-diffusive transport, we performed TAM measurements for various QDiP samples (Figure S8, S9) and compared the temporal evolution of diffusivity obtained at the lowest pump fluence (Figure 4a). The initial diffusivity decreases remarkably as

the inter-dot separation increases, and the super-diffusive regime is eliminated when CQDs are well separated by perovskite (perovskite loading of 90 vol%). We attribute the slower initial propagation to the reduced strength of electronic coupling and a lower degree of delocalisation. Intriguingly, at perovskite loading of 40 vol% – the inter-dot separation and exciton peak position do not change noticeably – a higher diffusivity is obtained (D = 106 cm^2 s^{-1}) compared to the pure CQD solids (Figure 4c). We suggest that this effect may arise either due to enhanced dielectric screening among dots[36] or improved structural uniformity of the film. These observations support the strong correlation between the initial transport regime and the extent of electronic coupling, which can be tuned by modifying the inter-particle spacing and matrix composition.

We also observed that the onset of the sub-diffusive regime is delayed as the perovskite percentage increases. The reciprocal persistence time of super-diffusive regime, $1/\tau_{super\text{-}diffusive}$, follows the same trend as the inhomogeneous broadening width (Figure 4d). This suggests that the energetic disorder tends to disrupt the super-diffusive transport regime[37], following which the system moves to a sub-diffusive regime mediated by Auger-assisted or normal hopping processes.

Our results illustrate that in a disordered system with a limited extent of delocalisation, super-diffusive transport and hopping-type transport can occur sequentially. We observed a volcano trend in the distance of super-diffusive transport as a function of perovskite content (Figure 4b). At 40 vol% perovskite loading, the largest super-diffusive transport length of ~90 nm is obtained, which corresponds to ~30 dots on average. The super-diffusive transport length is about a third of the thickness of an active layer used in photodetectors or solar cells, suggesting that the super-diffusive regime is of significant relevance to device operation.

CONCLUSION

In this work, we report a multi-stage carrier transport mechanism in both CQD and QDiP solids. We observed an initial super-diffusive transport that strongly correlates with the extent of carrier delocalisation and energetic disorder, followed by an Auger-assisted sub-diffusive transport before the carriers reach thermal equilibrium with the lattice, and a final hopping regime for the cooled carriers. This study introduces promising strategies to harness non-equilibrium transport processes for more efficient optoelectronic devices, and calls for new theoretical models to elucidate the limits of delocalised transport in CQDs. These findings provide new insights into the ultrafast dynamics in CQD solids and heterostructures and offer guidelines for future material optimisation and device engineering.

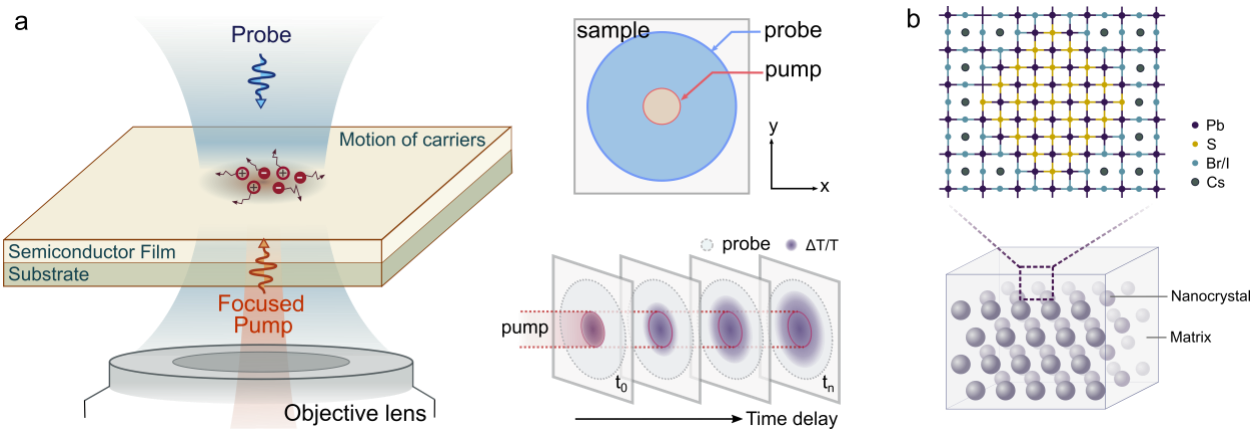

Figure 1. Schematics of femtosecond transient absorption microscopy and QDiP solids. a, Schematics of TAM setup. A near-diffraction-limited (σ of 133 nm) and transform-limited (9.2 fs, 580 nm) pump pulse is focused onto the sample through a high numerical aperture microscope objective. A loosely focused (σ of 6.4 μm) probe pulse is focused from the top onto the sample, and the transmitted probe is collected by the objective and imaged onto a digital camera. Comparing the recorded spatial distribution of carrier population at different time delays enables us to track the evolution of photoinduced dynamics with ~10 fs time resolution and ~10 nm spatial precision, which is limited merely by the signal-to-noise characteristics of the system. b, Schematic depiction of the atomistic model of a QDiP heterostructure. The $CsPbBr_2I$ matrix achieves an ideal lattice matching with embedded PbS CQDs, resulting in epitaxially-aligned interfaces.

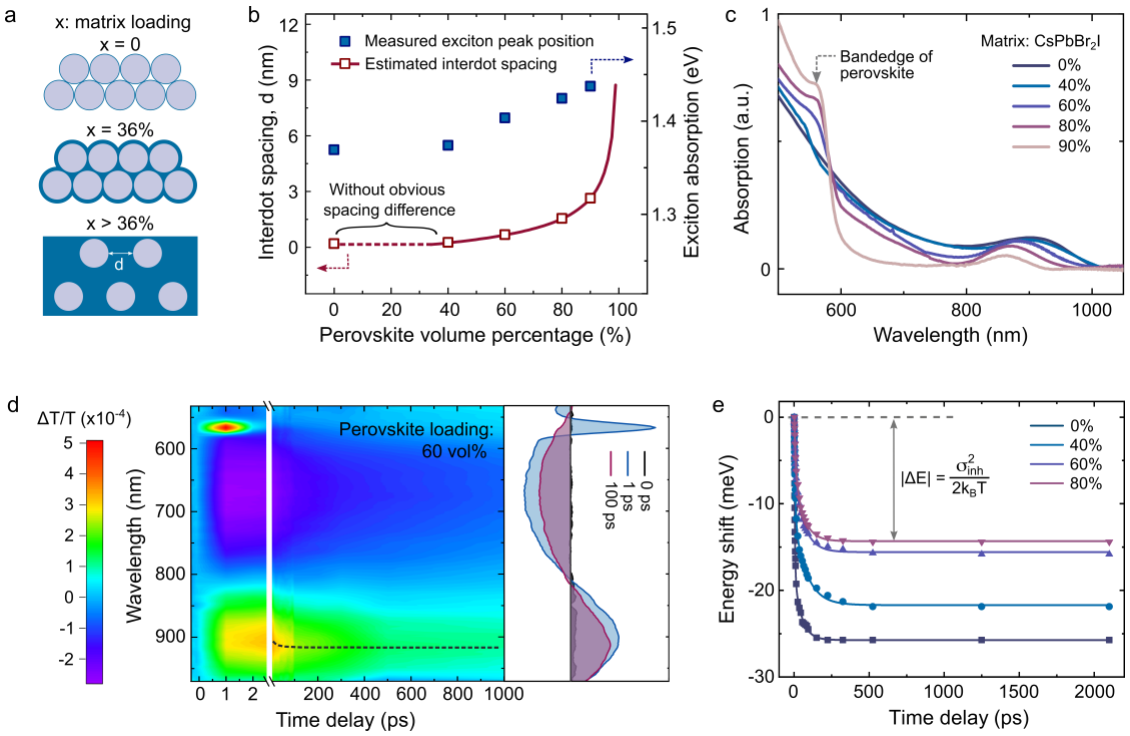

Figure 2. Structural and photophysical properties of QDiP solids. (a,b) Inter-dot spacing (red open squares) and exciton absorption peak position (blue-filled squares) as a function of perovskite volume percentage. Without the introduction of perovskite, halide-capped PbS CQDs form randomly-packed ensembles with a high packing density (~64%) and a tiny inter-dot separation (2 – 4 Å). At low perovskite loadings (< 36 vol%), perovskites fill in the voids among CQDs without noticeably separating the dots. At high perovskite loadings (> 36 vol%), increased inter-dot spacing results in a blue-shift of PbS exciton absorption peak. (c) Matrix-tuned absorption spectra of CQD:perovskite heterostructures. (d) Representative transient transmission map for QDiP solids (perovskite volume percentage is 60%). The black dashed line depicts the shift in the peak position of CQD transient bleach as a function of time. (e) The shifts of CQD bleach peak energy over time for pure CQDs and QDiP heterostructures with various perovskite concentrations. The symbols represent the experimental values and the solid lines are fits to an exponential decay function. The red-shift of the CQD bleach peak demonstrates that photoexcited carriers funnel to the lower-energy sites in films. The final energy shift, ΔE, is determined by the energetic disorder and available thermal activation.

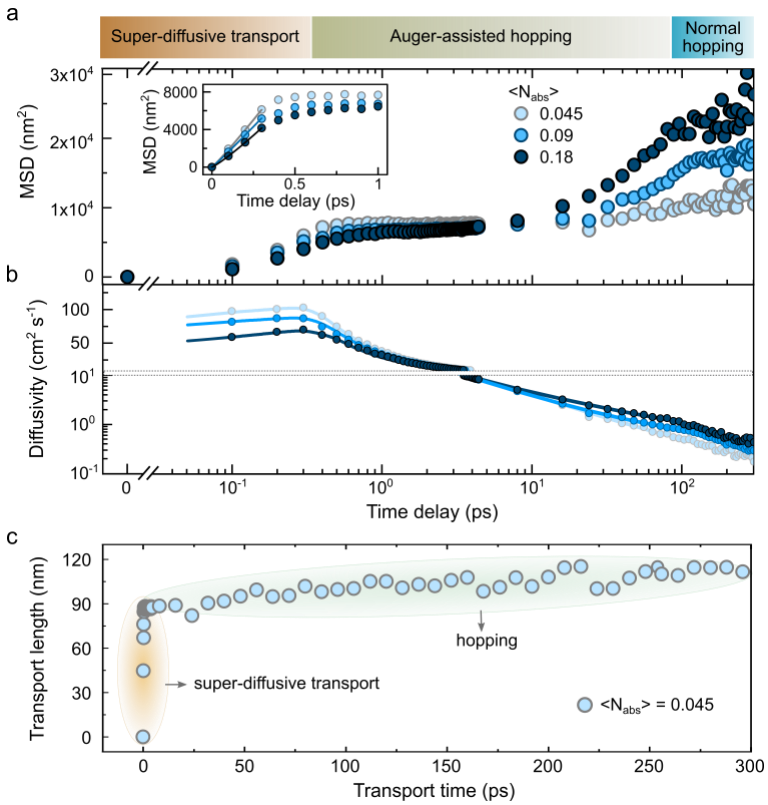

Figure 3. Dynamics of carrier propagation in pure CQD solids. (a) Time evolution of MSD ($\sigma_t^2 - \sigma_0^2$) for pure CQD solids measured at different excitation intensities. $\langle N_{abs} \rangle$ represents the average number of photons absorbed per CQD. The transport is divided into three regimes: super-diffusive transport, Auger-assisted hopping, and thermally activated hopping. The inset figure shows a zoom-in view for the early time range (< 1 ps), and fitted results are shown in solid lines to indicate a super-diffusive transport during the initial hundreds of femtoseconds. (b) Effective diffusivity as a function of time. Experimental values are displayed as symbols, while the fitted data are displayed as solid lines. (c) Time evolution of carrier transport length, $\sqrt{\sigma_t^2 - \sigma_0^2}$, in CQD solids obtained at low pump fluence ($\langle N_{abs} \rangle$ = 0.045). Carriers rapidly migrate over ~80 nm within ~300 fs. The initial fast transport regime is followed by a much slower transport at longer time delays. This indicates a distinct transition from super-diffusive transport to hopping-type transport.

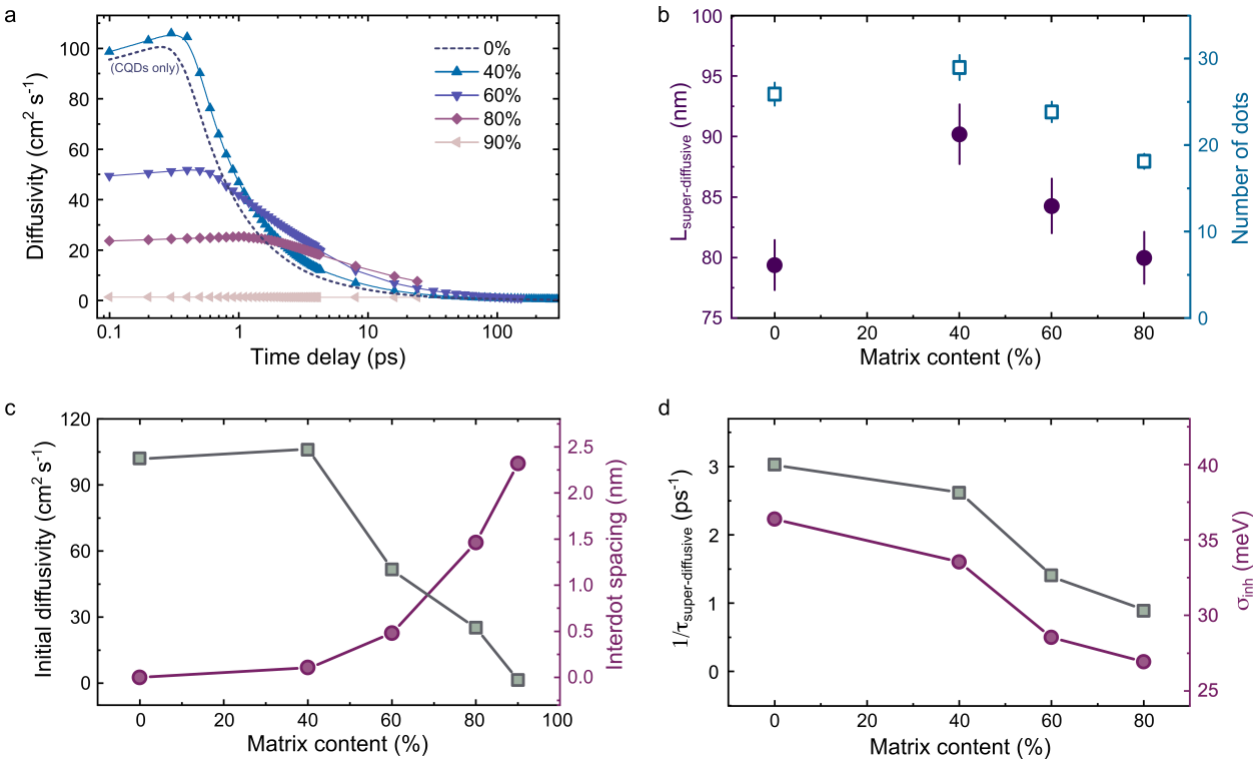

Figure 4. Carrier transport in QDiP solids at low pump fluence. a, Time evolution of diffusivity for QDiP heterostructures with various perovskite volume percentages. The dashed line represents the diffusivity for pure CQD control. b, Carrier transport length, $L_{super\text{-}diffusive}$ ($\sqrt{\sigma_t^2 - \sigma_0^2}$), and the corresponding number of dots for the super-diffusive region as a function of perovskite volume percentage. c, The maximum diffusivity and inter-dot spacing as a function of perovskite volume percentage. d, Reciprocal persistence time of super-diffusive regime, $1/\tau_{super\text{-}diffusive}$, and inhomogeneous broadening of site energy, σ_{inh}, as a function of perovskite volume percentage.

TOC GRAPHIC

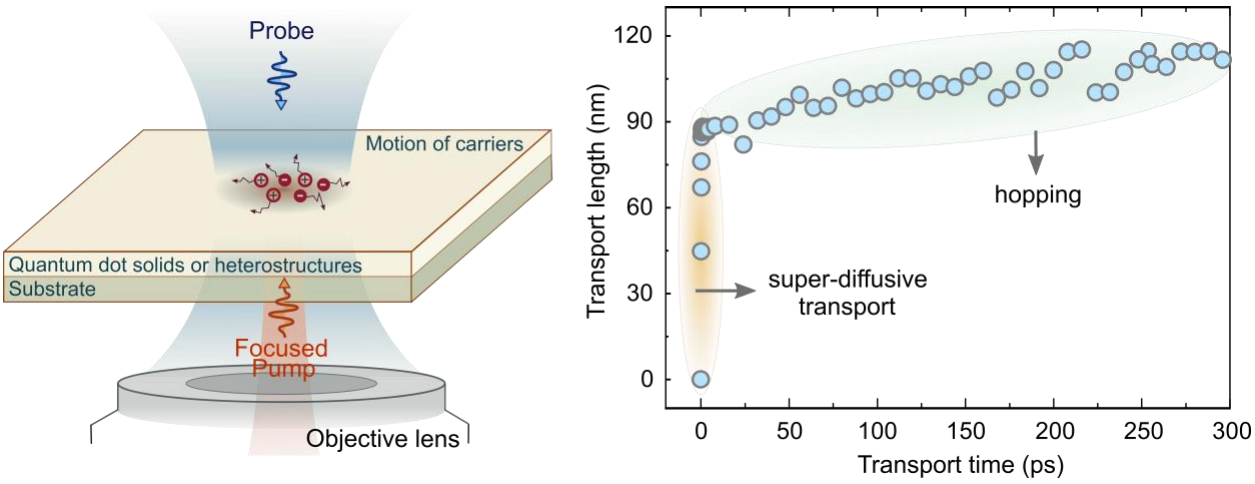

ASSOCIATED CONTENT

Supporting Information

Experimental methods, supplementary figures, and additional discussions are provided. This material is available free of charge via the Internet at http://pubs.acs.org.

AUTHOR INFORMATION

Corresponding Author

js2377@cam.ac.uk (J.S.); ar525@cam.ac.uk (A.R.)

Author Contributions

The manuscript was written through contributions of all authors. M.L., J.S. and A.R. designed the study. M.L. and J.S. contributed to all the experimental work. S.D.V. carried out the transient absorption spectroscopy measurement. Z.Z. synthesized the colloidal nanocrystals. A.R. supervised the project. M.L., J.S. and A.R. wrote the manuscript. All authors discussed the results and assisted in the preparation of the manuscript.

Funding Sources

This project has received funding from the European Research Council (ERC) under the European Union's Horizon 2020 research and innovation programme (grant agreement no. 758826). We acknowledge support from the Engineering and Physical Sciences Research Council (EPSRC) and the Winton Programme for the Physics of Sustainability. J.S. acknowledge support from the DGIST Start-up Fund Program of the Ministry of Science and ICT (2021070009).

ACKNOWLEDGMENT

The authors thank J. Xiao for his help during the course of this study.

ABBREVIATIONS

Colloidal quantum dot, CQD; Quantum-dot-in-perovskite, QDiP; Photoluminescence, PL; Transient absorption microscopy, TAM; Ground-state bleach, GSB; Photoinduced absorption, PIA.

REFERENCES

1. Ekimov, A. I.; Efros, Al. L.; Onushchenko, A. A. Quantum size effect in semiconductor microcrystals. *Solid State Commun.* **1985**, *56*, 921–924.
2. Brus, L. E. Electron–electron and electron-hole interactions in small semiconductor crystallites: the size dependence of the lowest excited electronic state. *J. Chem. Phys.* **1984**, *80*, 4403–4409.
3. Yazdani, N.; Bozyigit, D.; Yarema, O.; Yarema, M.; Wood, V. Hole mobility in nanocrystal solids as a function of constituent nanocrystal size. *J. Phys. Chem. Lett.* **2014**, *5*, 3522–3527.

4. Gilmore, R. H. Lee, E. M. Y.; Weidman, M. C.; Willard, A. P.; Tisdale, W. A. Charge carrier hopping dynamics in homogeneously broadened PbS quantum dot solids. *Nano Lett.* **2017**, *17*, 893–901.
5. Liu, M.; Voznyy, O.; Sabatini, R.; García de Arquer, F. P.; Munir, R.; Balawi, A. H.; Lan, X.; Fan, F.; Walters, G.; Kirmani, A. R.; Hoogland, S.; Laquai, F.; Amassian, A.; Sargent, E. H. Hybrid organic–inorganic inks flatten the energy landscape in colloidal quantum dot solids. *Nat. Mater.* **2017**, *16*, 258–263.
6. Ning, Z.; Gong, X.; Comin, R.; Walters, G.; Fan, F.; Voznyy, O.; Yassitepe, E.; Buin, A.; Hoogland, S.; Sargent, E. H. Quantum-dot-in-perovskite solids. *Nature* **2015**, *523*, 324–328.
7. Voznyy, O.; Sutherland, B.; Ip, A.; Zhiotomirsky, D.; Sargent, E. H. Engineering charge transport by heterostructuring solution-processed semiconductors. *Nat. Rev. Mater.* **2017**, *2*, 17026.
8. Saidaminov, M. I.; Adinolfi, V.; Comin, R.; Abdelhadv, A. L.; Peng, W.; Dursun, I.; Yuan, M.; Hoogland, S.; Sargent, E. H.; Bakr, O. M. Planar-integrated single-crystalline perovskite photodetectors. *Nat. Commun.* **2015**, *6*, 8724.
9. Liu, M.; Chen, Y.; Tan, C.-S.; Quintero-Bermudez, R.; Proppe, A. H.; Munir, R.; Tan, H.; Voznyy, O.; Scheffel, B.; Walters, G.; Kam, A. P. T.; Sun, B.; Choi, M.-J.; Hoogland, S.; Amassian, A.; Kelley, S. O.; García de Arquer, F. P.; Sargent, E. H. Lattice anchoring stabilizes solution-processed semiconductors. *Nature* **2019**, *570*, 96–101.
10. Gong, X.; Yang, Z.; Walters, G.; Comin, R.; Ning, Z.; Beauregard, E.; Adinolfi, V.; Voznyy, O.; Sargent, E. H. Highly efficient quantum dot near-infrared light-emitting diodes. *Nat. Photonics* **2016**, *10*, 253–257.

11. García de Arquer, F.; Gong, X.; Sabatini, R. P.; Liu, M.; Kim, G.-H.; Sutherland, B. R.; Voznyy, O.; Xu, J.; Pang, Y.; Hoogland, S.; Sinton, D.; Sargent, E. H. Field-emission from quantum-dot-in-perovskite solids. *Nat. Commun.* **2017**, *8*, 14757.
12. Proppe, A. H.; Xu, J.; Sabatini, R. P.; Fan, J. Z.; Sun, B.; Hoogland, S.; Kelley, S. O.; Voznyy, O.; Sargent, E. H. Picosecond charge transfer and long carrier diffusion lengths in colloidal quantum dot solids. *Nano Lett*. **2018**, *18*, 7052–7059.
13. AkseIrod, G. M.; Prins, F.; Poulikakos, L. V.; Lee, E. M. Y.; Weidman, M. C.; Mork, A. J.; Willard, A. P.; Bulović, V.; Tisdale, W. A. Subdiffusive exciton transport in quantum dot solids. *Nano Lett.* **2014**, *14*, 3556−3562.
14. Choi, J.-H.; Fafarman, A. T.; Oh, S. J.; Ko, D.-K.; Kim, D. K.; Diroll, B. T.; Muramoto, S.; Gillen, J. G.; Murray, C. B.; Kagan, C. R. Bandlike transport in strongly coupled and doped quantum dot solids: A route to high-performance thin-film electronics. *Nano Lett.* **2012**, *12*, 2631−2638.
15. Lan, X.; Chen, M.; Hudson, M. H.; Kamysbayev, V.; Wang, Y.; Guyot-Sionnest, P.; Talapin, D. V. Quantum dot solids showing state-resolved band-like transport. *Nat. Mater.* **2020**, *19*, 323–329.
16. Gesuele, F.; Sfeir, M. Y.; Koh, W.-K.; Murray, C. B.; Heinz, T. F.; Wong, C. W. Ultrafast supercontinuum spectroscopy of carrier multiplication and biexcitonic effects in excited states of PbS quantum dots. *Nano Lett.* **2012**, *12*, 2658–2664.
17. EI-Ballouli, A. O.; Alarousu, E.; Usman, A.; Pan, J.; Bakr, O. M.; Mohammed, O. F. Real-time observation of ultrafast intraband relaxation and exciton multiplication in PbS quantum dots. *ACS Photonics* **2014**, *1*, 285–292.

18. Zhang, C.; Do, T. N.; Ong, X.; Chan, Y.; Tan, H.-S. Understanding the features in the ultrafast transient absorption spectra of CdSe quantum dots. *Chem. Phys.* **2016**, *481*, 157-164.
19. Bassler, H. Charge transport in disordered organic photoconductors – a Monte-Carlo simulation study. *Phys. Stat. Sol. B* **1993**, *175*, 15−56.
20. Diezmann, A. V.; Shechtman, Y.; Moerner, W. E. Three-dimensional localization of single molecules for super-resolution imaging and single-particle tracking. *Chem. Rev.* **2017**, *117*, 7244–7275.
21. Schnedermann, C.; Sung, J.; Pandya, R.; Verma, S. D.; Chen, R. Y. S.; Gauriot, N.; Bretscher, H. M.; Kukura, P.; Rao, A. Ultrafast tracking of exciton and charge carrier transport in optoelectronic materials on the nanometer scale. *J. Phys. Chem. Lett.* **2019**, *10*, 6727–6733.
22. Sung, J.; Schnedermann, C.; Ni, L.; Sadhanala, A.; Chen, R. Y. S.; Cho, C.; Priest, L.; Lim, J. M.; Kim, H.-K.; Monserrat, B.; Kukura, P.; Rao, A. Long-range ballistic propagation of carriers in methylammonium lead iodide perovskite thin films. *Nat. Phys.* **2020**, *16*, 171–176.
23. Schnedermann, C.; Lim, J. M.; Wende, T.; Duarte, A. S.; Ni, L.; Gu, Q.; Sadhanala, A.; Rao, A.; Kukura, P. Sub-10 fs time-resolved vibronic optical microscopy. *J. Phys. Chem. Lett.* **2016**, *7*, 4854–4859.
24. Gao, J.; Fidler, A.; Klimov, V. Carrier multiplication detected through transient photocurrent in device-grade films of lead selenide quantum dots. *Nat. Commun.* **2015**, *6*, 8185.

25. Cademartiri, L.; Montanari, E.; Calestani, G.; Migliori, A.; Guagliardi, A.; Ozin, G. A. Size-dependent extinction coefficients of PbS quantum dots. *J. Am. Chem. Soc.* **2006**, *128*, 10337–10346.

26. Moreels, I.; Lambert, K.; Smeets, D.; Muynck, D. D.; Nollet, T.; Martins, J. C.; Vanhaecke, F.; Vantomme, A.; Delerue, C.; Allan, G.; Hens, Z. Size-dependent optical properties of colloidal PbS quantum dots. *ACS Nano* **2009**, *3*, 3023–3030.

27. Guo, Z.; Manser, J. S.; Wan, Y.; Kamat, P. V.; Huang, L. Spatial and temporal imaging of long-range charge transport in perovskite thin films by ultrafast microscopy. *Nat. Commun.* **2015**, *6*, 7471.

28. Sun, B.; Voznyy, O.; Tan, H.; Stadler, P.; Liu, M.; Walters, G.; Proppe, A. H.; Liu, M.; Fan, J.; Zhuang, T.; Li, J.; Wei, M.; Xu, J.; Kim, Y.; Hoogland, S.; Sargent, E. H. Pseudohalide-exchanged quantum dot solids achieve record quantum efficiency in infrared photovoltaics. *Adv. Mater.* **2017**, *29*, 1700749.

29. Allgaier, R. S. Mobility of electrons and holes in PbS, PbSe, and PbTe between room temperature and 4.2°K. *Phys. Rev.* **1958**, *111*, 1029-1037.

30. Cho, B.; Peters, W. K.; Hill, R. J.; Courtney, T. L.; Jonas, D. M. Bulklike Hot Carrier Dynamics in Lead Sulfide Quantum Dots. *Nano Lett.* **2010**, 10, 2498–2505.

31. Chen, T.; Reich, K. V.; Kramer, N. J.; Fu, H.; Kortshagen, U. R.; Shklovskii, B. I. Metal–insulator transition in films of doped semiconductor nanocrystals. *Nat. Mater.* **2015**, *15*, 299.

32. Klimov, V. I. Optical nonlinearities and ultrafast carrier dynamics in semiconductor nanocrystals. *J. Phys. Chem. B* **2000**, *104*, 6112–6123.

33. Shabaev, A.; Efros, A. L.; Efros, A. L. Dark and photo-conductivity in ordered array of nanocrystals. *Nano Lett.* **2013**, *13*, 5454–5461.

34. Gao, J.; Kidon, L.; Rabani, E.; Alivisatos, A. P. Ultrahigh hot carrier transient photocurrent in nanocrystal arrays by auger recombination. *Nano Lett.* **2019**, *19*, 4804–4810.
35. Gilmore, R. H.; Liu, Y.; Shcherbakov-Wu, W.; Dahod, N.; Lee, E.; Weidman, M.; Li, H.; Jean, J.; Bulović, V.; Willard, A.; Grossman, J. C.; Tisdale, W. Epitaxial dimers and Auger-assisted detrapping in PbS quantum dot solids. *Matter* **2019**, *5*, 1692–1694.
36. Hou, X.; Kang, J.; Qin, H.; Chen, X.; Ma, J.; Zhou, J.; Chen, L.; Wang, L.; Wang, L.-W.; Peng, X. Engineering Auger recombination in colloidal quantum dots via dielectric screening. *Nat. Commun.* **2019**, *10*, 1750.
37. Moix, J.; Khasin, M.; Cao, J. Coherent quantum transport in disordered systems: I. The influence of dephasing on the transport properties and absorption spectra on one-dimensional systems. *New J. Phys.* **2013**, *15*, 085010.